Cohesive zone modelling of hydrogen induced cracking on the interface of clad steel pipes

L. Jemblie[a,*], V. Olden[b], P. Mainçon[b], O. M. Akselsen[a,b]

[a] *Department of Mechanical and Industrial Engineering, NTNU, 7491 Trondheim, Norway*
[b] *SINTEF Materials and Chemistry, 7465 Trondheim, Norway*

Abstract

A coupled finite element and cohesive zone modelling approach has been applied to simulate hydrogen induced fracture initiation in a hot rolled bonded clad steel pipe. The results are compared in terms of experimental fracture mechanical testing in air and under in situ electrochemical hydrogen charging. A best fit to the experimental CTOD fracture initiation toughness value in air was achieved for an initial cohesive stiffness $k_n = 4 \cdot 10^6$ MPa/mm and a critical cohesive stress $\sigma_c = 1210$ MPa. For simulating under hydrogen influence, the hydrogen induced lowering of the cohesive strength was computed both in terms of the lattice concentration and the total hydrogen concentration. Two different formulations for calculating the dislocation trap density was considered. The simulated results revealed that both hydrogen in lattice and hydrogen trapped at dislocations can be responsible for the observed hydrogen induced reduction in CTOD fracture initation toughness. The choice of trap density formulation appeared significant only under the assumption that both lattice and trapped hydrogen infer an influence on the hydrogen induced lowering of the cohesive strength. Further effort is needed to provide a reliable description of the interface hydrogen content and distribution, providing a model able to transfer between different material systems.

Keywords: Hydrogen embrittlement, Hydrogen diffusion, Cohesive zone modelling, Clad pipe, Cladding

1. Introduction

Transport of unprocessed oil and gas requires pipelines with a corrosion resistant interior, able to withstand environmental degradation and cracking during full service life. Clad pipes, where a corrosion resistant alloy (CRA) is internally bonded to a conventional carbon steel pipe, have become increasingly popular as an economical viable option for corrosion management, combining the mechanical properties of the structural steel with the corrosive properties of the CRA. This however offers new challenges with respect to integrity management and degradation assessment, due to an inhomogeneous material combination and a complex interface region.

The carbon steel base metal (BM) and the austenitic CRA are joined by hot-roll bonding of bi-material plates, followed by bending into the shape of a pipe in a press bending process [1, 2]. During production, due to the wide difference in chemical composition between the base metal and the CRA, considerable transport of elements across the interface may occur. The resulting microstructure has proven complex, with increased hardness and carbide precipitates on the clad side and carbon depletion followed by grain growth in the ferritic base metal [3, 4, 5, 6].

The presence of inter metallic compounds, hard zones and residual stresses may significantly deteriorate the dissimilar interface, increasing the pipe's susceptibility to corrosion or hydrogen embrittlement. The interfacial zone it-

*Corresponding author
Email address: lise.jemblie@ntnu.no (L. Jemblie)

self represents an area with large potential for increased hydrogen concentration, as hydrogen atoms are prone to accumulate at precipitates and in areas of increased hydrostatic stresses. Recently a series of failures on cathodically charged subsea dissimilar welds have been attributed to hydrogen embrittlement, where the presence of carbide precipitates at the interface resulted in a microstructure particularly sensitive to hydrogen induced failures [7, 8].

Hydrogen induced degradation of mechanical properties is a well recognized threat to the structural integrity of subsea applications, with several reported incidents. It manifests as loss in ductility, strength and toughness, which may result in unexpected and premature catastrophic failures. In subsea pipeline applications, the main sources of hydrogen are electrochemical reduction of water resulting from cathodic protection and the presences of moisture during welding.

In previous work by the present authors [9], the hydrogen embrittlement susceptibility of 316L austenitic stainless steel - X60 carbon steel hot roll bonded clad pipes was investigated through compact tension (CT) fracture mechanical testing in air and under in situ electrochemical hydrogen charging. The experimental procedure and relevant findings are summarised in Section 2 and 3 of this paper.

In the present study, a combined experimental and finite element (FE) cohesive zone modelling (CZM) approach for prediction of hydrogen induced fracture initiation in a hot roll bonded clad steel pipe is proposed. The developed model is based on coupled effects between mechanical quantities and hydrogen mass diffusion. CZM provides a phenomenological continuum framework for failure analysis, not representative of any physical material. It has in recent years gained increasing interest as a suitable method for modelling hydrogen embrittlement [10, 11, 12, 13, 14]. The damage process is classically described by interface elements, which constitutive relation is defined by a so-called traction separation law (TSL) [15]. The hydrogen transport is described by an enhanced diffusion model, accounting for trapping by dislocations and hydrostatic drift [16, 17], while the deleterious effect of hydrogen on the accelerated material damage is represented by a lowering of the cohesive energy at failure. A review on coupled diffusion and cohesive zone modelling as an approach for numerically assessing hydrogen embrittlement in steel structures has previously been published [18].

To date, the effect of trapping on hydrogen induced fracture remains controversial and there is no consensus as to whether hydrogen in lattice or hydrogen trapped at microstructural defects is the dominant source of embrittlement. In the current work, the hydrogen induced lowering of the cohesive strength is computed both in terms of the lattice concentration and the total concentration, where two different models for calculating the dislocation trap densities are considered. The main objective is to investigate the models capability of predicting hydrogen induced fracture. All simulated results are discussed in terms of the experimental findings.

2. Experimental procedure

2.1. Materials

The clad steel pipe investigated in this study consist of API X60 pipeline steel as the base material and austenitic stainless steel grade 316L as the clad, presented in Table 1. The chemical composition, tensile properties and Vickers hardness (HV10) are presented in Table 2.

Table 1: Investigated pipe sample.

		Thickness [mm]		
BM	Clad	Clad	Pipe wall	Pipe
X60	316L	3.0	15.7	16.0

The clad layer is bonded to the pipeline steel plate through hot rolling followed by quenching and tempering, before bent into the shape of a pipe in a press bending

Table 2: Chemical composition, tensile properties and Vickers hardness of the clad steels under investigation.

Steel	C	Si	Mn	P	S	Ni	Cr	Mo	Rp0.2 [MPa]	Rm [MPa]	HV10
X60	0.076	0.375	1.38	0.006	0.0008	0.27	0.024	0.003	493	595	241
316L	0.018	0.368	1.382	0.031	0.002	11.09	16.68	2.042	440	647	187

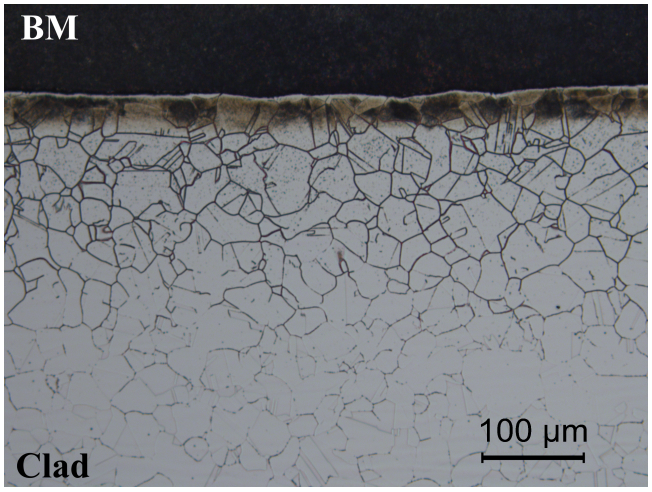

Figure 1: Interface microstructure [19].

manufacturing process. Specimens for investigation were extracted in the longitudinal direction of the pipes in as supplied condition. The interface microstructure is presented in Figure 1, where a continuous area of carbide precipitates (∼200 µm wide) is clearly visible on the clad side, attributed to carbon diffusion across the interface during production. Microhardness measurements (HV0.025) across the interface confirmed carbon diffusion, showing an average hardness level of about 350 HV on the clad side and 156 HV on the BM side [19].

2.2. Fracture mechanical testing

Constant load rate CT fracture mechanical testing was performed in air and under cathodic protection (CP), in order to establish CTOD (Crack Tip Opening Displacement)-R curves and values for crack initiation. CT specimens were machined with the notch tip at the dissimilar metal interface to an initial crack length to width ratio a_0/W of 0.5, using electro-discharge machining (EDM), as it was deemed impossible to produce a fatigue crack propagating exactly along the dissimilar interface. Details of the specimen geometry and dimensions are given in Figure 2. For comparative reasons and in order to verify the finite element model, fracture mechanical testing of pure BM CT specimens were also performed both in air and in hydrogen environment.

A constant loading rate of 0.74 N/min was applied, corresponding to a stress intensity rate of $6.8 \cdot 10^{-4}$ MPa $\mathrm{m}^{1/2}$/s. This is in accordance with previous work by Lee and Gangloff [20] on hydrogen assisted cracking of ultra-high strength martensitic steel, making the resulting fracture toughness independent of the loading rate. For testing in hydrogen environment, the specimens were immersed in a 3.5 % NaCl solution with an applied cathodic potential of -1050 $\mathrm{mV_{SCE}}$. Prior to test initiation, the specimens were hydrogen pre-charged in the test rig for 24 hours at -1050 $\mathrm{mV_{SCE}}$ in a 3.5 % NaCl solution. Pre-charging time was decided by diffusion calculations in the BM, based on the thick plate solution of Fick's law. All testing was performed at room temperature.

For determination of CTOD-R curves, a multiple specimen procedure was applied where the specimens were unloaded at different CTOD values in order to establish points on the curve for various crack extensions. The extent of stable crack growth was marked with heat tinting. After testing the samples were cracked open in liquid nitrogen, and the crack length and crack extension was measured at 5 equally spaced points across the sample, obtaining the original crack length and the mean crack extension.

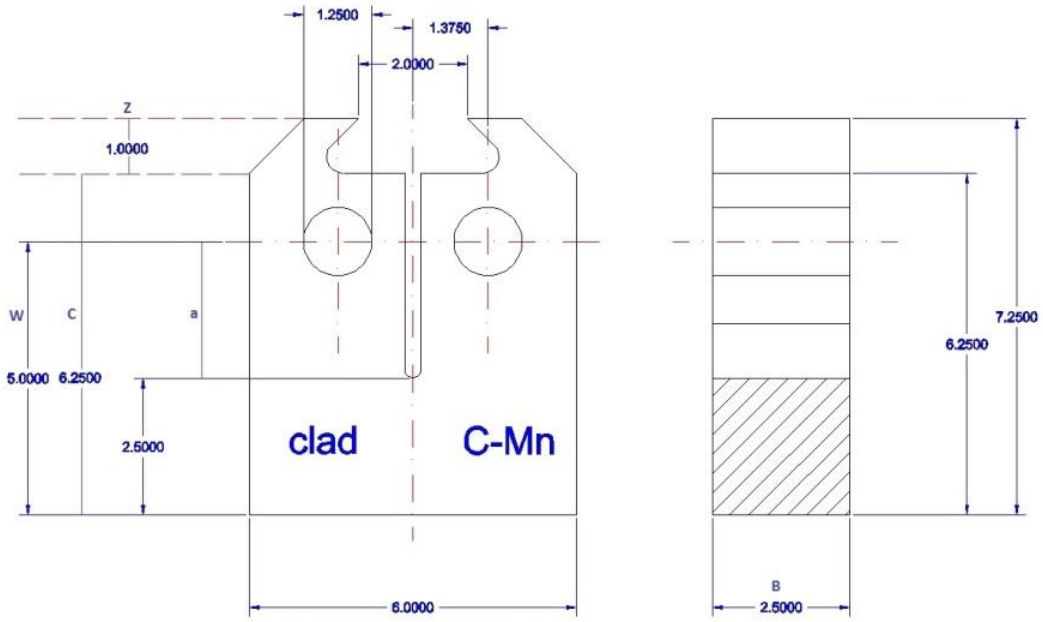

Figure 2: Compact tension specimen geometry and dimensions, W=5 mm, B=2.5 mm, a=2.5 mm, C=6.25 mm, z=1.0 mm, notch radius=0.15 mm.

2.2.1. Analysis of test data

During testing, the load and the machine displacement were recorded. For testing in air, a machined clip gage, made to fit the small size of the specimen, was used to measure the Crack Mouth Opening Displacement (CMOD) at the knife edges. As the use of clip gages was not possible for testing under CP, a correlation factor between displacement and CMOD for testing in air was used to obtain the CMOD curve for testing under CP. The average ratio between plastic CMOD (V_p) and plastic displacement (d_p), resulting from testing in air, was used to obtain the plastic CMOD under CP

$$V_{p,\mathrm{CP}} = \left(\frac{V_{p,\mathrm{air}}}{d_{p,\mathrm{air}}}\right) \cdot d_{p,\mathrm{CP}} \quad (1)$$

at the point of unloading. The CTOD-R curves were constructed following standard BS 7448-4 [21], with the fracture initiation toughness defined as the intersection between the R-curve and the analytical blunting line ($\delta_i = 1.87(R_m/R_{p0.2})\Delta a$).

3. Experimental test results

Detailed results from the fracture mechanical testing are previously reported in [9]. A summary of the main relevant findings are presented here.

Examples of resulting Load-CMOD curves are reported in Figure 3, including testing of both bi-material and pure BM specimens, denoted interface and BM respectively. Fairly consistent results were observed for all parallel tests. For testing in air, a reduction in both maximum attained load and corresponding CMOD level was observed for all bi-material specimens, indicating some degradation of the dissimilar interface and a lowering of the systems overall fracture resistance. For testing under CP, hydrogen influence was observed for both the BM and interface samples, with a reduction in maximum attained load and the corresponding CMOD level.

The resulting linear best fit CTOD-R curves are compared in Figure 4, illustrating again significant influence of hydrogen on the dissimilar interface fracture resistance. The corresponding fracture initiation toughness values are summarized in Table 3. As the J-integral and the stress

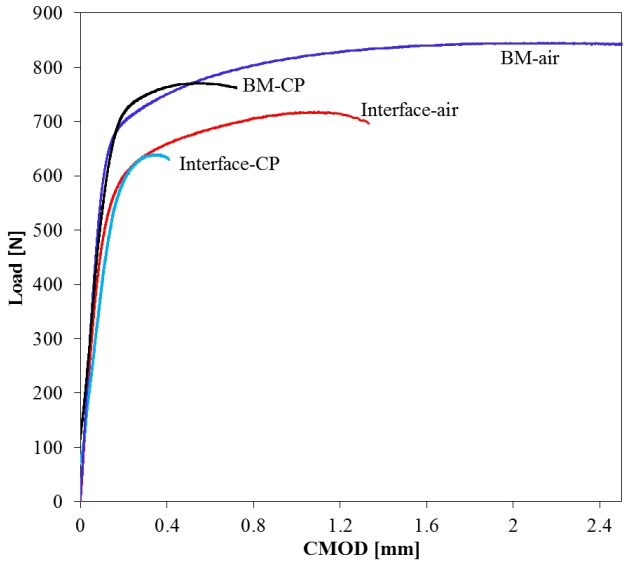

Figure 3: Load-CMOD for curves for bi-material (interface) and pure BM specimens, tested in air and under CP.

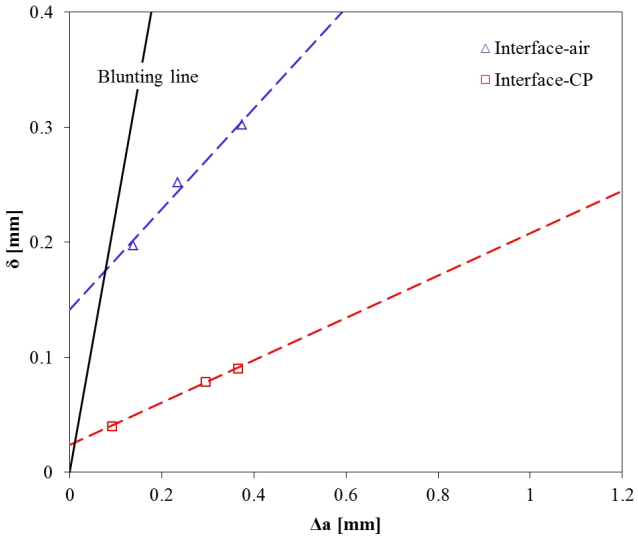

Figure 4: Linear best fit CTOD-R curves for the bi-material (interface) samples, tested in air and under CP.

Table 3: Fracture initiation toughness values for the bi-material (interface) samples, tested in air and under CP.

Env.	δ_i [mm]	$J^{a)}$ [N/mm]	$K_I^{b)}$ [MPa$\sqrt{m}$]
Air	0.176	173	199
CP	0.025	25	76

a) $J = 2\delta R_{p0.2}$

b) $K_I = \left(\frac{JE}{1-\nu^2}\right)^{1/2}$

intensity factor are more commonly cited fracture mechanical parameters, the values of the CTOD fracture initiation toughness were converted to J and K_I. Hydrogen was found to reduce the CTOD fracture initiation toughness with 85 % for the bi-material samples.

Light optical microscopy investigations of the fracture surface profiles revealed an alternating crack path, shifting between the dissimilar interface and the BM adjacent to the interface for both test environments, however crack propagation through the BM appeared dominant. The strong susceptibility of the ferritic BM to hydrogen embrittlement and degradation is consistent with general knowledge of hydrogen effects on pipeline steels. Scanning Electron Microscope (SEM) observations of the fracture surfaces supported the findings [9]; a dimpled morphology indicative of ductile fracture for the samples tested in air, and a distinct multifaceted appearance, indicative of cleavage fracture, for the samples tested under CP.

4. The model framework

The applied modelling approach simulates transient hydrogen diffusion, plastic deformation and material damage using cohesive elements, with the aim of reproducing the CTOD fracture initiation toughness. Crack growth analysis is beyond the scope of this work. In the following, the models and their respective couplings are outlined. A thorough review of the modelling approach has previously been published[18]. The applied finite element code was ABAQUS Standard version 6.13.

4.1. Hydrogen transport

Diffusion of atomic hydrogen is described by an enhanced transport model originally proposed by Sofonis and McMeeking [16] and subsequently modified by Krom et al. [17], accounting for trapping by dislocations and hydrostatic drift:

$$\frac{\partial C_L}{\partial t} + \frac{\partial C_T}{\partial t} - \nabla\cdot(D_L \nabla C_L) - \nabla\left(\frac{D_L \overline{V}_H}{RT} C_L \nabla p\right) = 0 \quad (2)$$

C_L is the hydrogen concentration in normal interstitial lattice sites (NILS), C_T is the hydrogen concentration in traps, D_L is the lattice diffusion coefficient, $\overline{V}_H$ is the partial molar volume of hydrogen and p is the hydrostatic pressure. The model distinguishes between two hydrogen atom populations; hydrogen in NILS (diffusible) and hydrogen trapped at dislocations. The C_L and C_T concentrations are related to the hydrogen lattice and trap sites occupancy θ_L and θ_T through

$$C_L = \theta_L N_L \tag{3}$$

$$C_T = \theta_T N_T \tag{4}$$

where N_L and N_T are the density of lattice and trap sites, respectively. Assuming rapid trapping and detrapping kinetics, hydrogen in NILS and hydrogen in reversible trapping sites are considered always to be in local equilibrium, a theory originally developed by Oriani [22]. As such

$$\frac{\theta_T}{1-\theta_T} = \frac{\theta_L}{1-\theta_L} \exp\left(\frac{E_B}{RT}\right) \tag{5}$$

with E_B being the trap binding energy. The lattice and trapped hydrogen concentrations can then be related through

$$C_T = \frac{K_T N_T C_L}{N_L + C_L(K_T - 1)} \tag{6}$$

where K_T denotes the equilibrium constant, as defined by the exponential term in Eq. 5.

The number of lattice sites N_L is related to the properties of the host metal [17]:

$$N_L = \frac{N_A \beta}{V_M} \tag{7}$$

where V_M is the molar volume of the metal, N_A is the Avogadro constant and β is the number of interstitial lattice sites per metal atom. The number of trap sites N_T varies point-wise dependent on the local plastic strain level. In the present work, two different models for calculating the trap density are considered. The first model is according to the experimental work of Kumnick and Johnson [23], relating the dislocation trap density to the amount of plastic strain [16, 17]

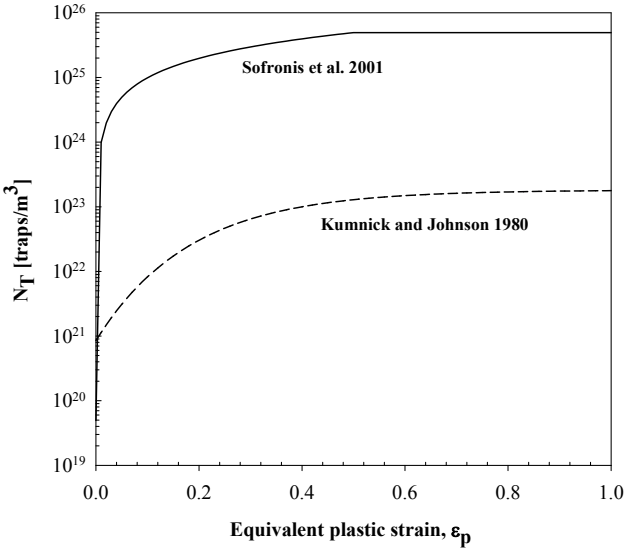

Figure 5: Dislocation trap density models by Kumnick and Johnson [23] and Sofronis et al. [24, 25].

$$\log N_T = 23.26 - 2.33 \exp(-5.5\varepsilon_p) \tag{8}$$

where ε_p is the equivalent plastic strain. The second model, originally suggested by Sofronis et al. [24, 25], assumes one trap site per atomic plane threaded by a dislocation. The dislocation trap density is then expressed as a function of the dislocation density ρ and the lattice parameter a:

$$N_T = \sqrt{2}\frac{\rho}{a} \tag{9}$$

The dislocation density (measured in dislocation line length per cubic meter) is considered to vary linearly with the equivalent plastic strain according to

$$\rho = \begin{cases} \rho_0 + \gamma\varepsilon_p & \text{for } \varepsilon_p < 0.5 \\ 10^{16} & \text{for } \varepsilon_p \geq 0.5 \end{cases} \tag{10}$$

where $\rho_0 = 10^{10}$ line length/m^3, denotes the dislocation density at zero plastic strain, and $\gamma = 2.0{\cdot}10^{16}$ line length/m^3. Figure 5 compares the two dislocation trap density model approaches. It can be concluded that the model by Sofronis et al. yields a dislocation trap density about three orders of magnitude larger than the data by Kumnick and Johnson.

Equation (2) describes the coupling between mass transport and local mechanical field quantities through a stress and strain depended diffusion process, predicting an accumulation of hydrogen in areas of high hydrostatic stress and plastic strain. Once C_L is known by solving Eq. (2), C_T can be obtained from Eq. 6, with N_L taken from Eq. (7) and N_T taken from Eq. (8) - (10). The diffusivity D_L and trap binding energy E_B are given as input parameters.

The above hydrogen diffusion formulation is implemented in ABAQUS through the user subroutine UMATHT, taking advantage of the analogy between heat and mass diffusion equations, treating the solute concentration as temperature. The FEM formulation for hydrogen diffusion as well as the implementation in ABAQUS using UMATHT is described in [26].

4.2. Elastic plastic stress analysis

The elastic plastic stress analysis is performed using the standard von Mises material model in ABAQUS Standard with a material specific stress strain curve representative of the ferritic base material and the austenitic clad.

4.3. The cohesive model

Material damaged is modelled by cohesive elements, implemented along the prospective crack path. The cohesive elements constitutive response is described by a traction separation law (TSL), characterizing the separation process by describing the forces opposing crack formation (tractions) as a function of the incipient crack surfaces' separation distance. Common to most TSLs is that they can be described by two independent parameters out of the following three: the critical cohesive stress σ_c, the critical separation δ_c and the cohesive energy Γ_c. In the present work, a polynomial TSL originally proposed by Needleman [15] is used:

$$\sigma(\delta) = \begin{cases} \frac{27}{4}\sigma_c \frac{\delta}{\delta_c}\left(1 - \frac{\delta}{\delta_c}\right)^2 & \text{for } \delta < \delta_c \\ 0 & \text{for } \delta \geq \delta_c \end{cases} \tag{11}$$

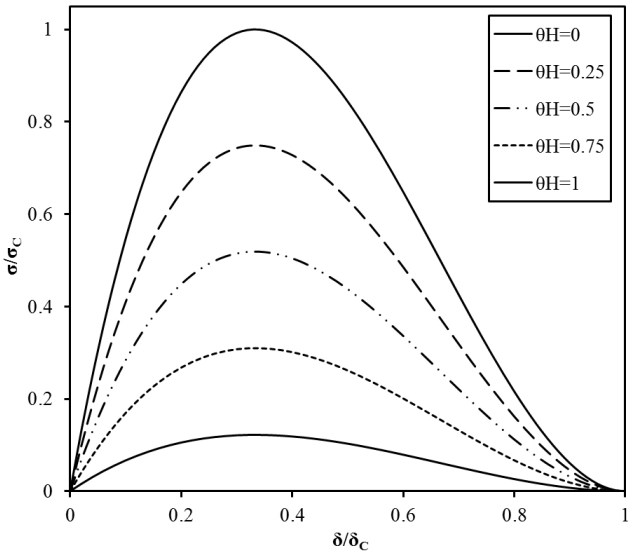

Figure 6: Normalised polynomial traction separation law for various levels of hydrogen coverage.

where the area embedded by the curve represents the cohesive energy, calculated from

$$\Gamma_c = \frac{9}{16}\sigma_c \delta_c \tag{12}$$

The influence of hydrogen is accounted for by a decrease in the critical cohesive stress with increasing hydrogen coverage θ_H. In the present work, a relationship originally proposed by Serebrinsky et al. [10] is applied, based on first principle calculations by Jiang and Carter [27] on ideal cleavage energies of bcc iron in the presence of various amounts of hydrogen, giving the following coupling between hydrogen coverage and the critical hydrogen dependent cohesive stress $\sigma_c(\theta_H)$:

$$\frac{\sigma_c(\theta_H)}{\sigma_c(0)} = 1 - 1.0467\theta_H + 0.1687\theta_H^2 \tag{13}$$

$\sigma_c(0)$ is the critical cohesive stress with no hydrogen influence. Figure 6 graphically illustrates the polynomial TSL in Equation (11) for various levels of hydrogen coverage.

The definition of hydrogen coverage θ_H follows the Langmuir-McLean isotherm [28], relating it to the bulk hydrogen concentration C (unit mol H/mol Fe) through

$$\theta_H = \frac{C}{C + \exp(-\Delta G_b^0 / RT)} \tag{14}$$

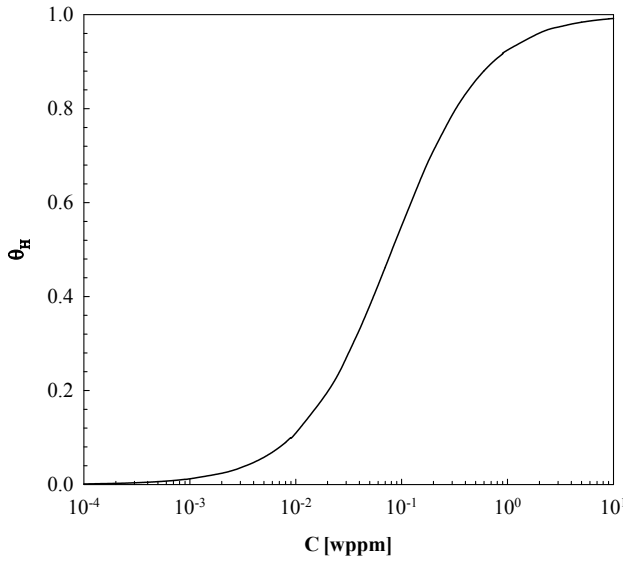

Figure 7: Hydrogen coverage θ_H as a function of the hydrogen concentration C, plotted according to the Langmuir-McLean isotherm for $\Delta G_b^0 = 30$ kJ/mol.

where ΔG_b^0 is the Gibbs energy difference between surface and bulk material, surface being any microstructural interface like crystallographic plane, grain boundary etc. Figure 7 plots the hydrogen coverage θ_H as a function of the hydrogen concentration C, assuming $\Delta G_b^0 = 30$ kJ/mol as suggested by Serebrinsky et al. [10].

5. Simulation of CT specimen

5.1. FE model

A 2D representation of the bi-material CT specimen in Figure 2 is applied for the finite element analysis. Details of the model domain are given in Figure 8. All dimension are identical to the experimental test samples. The elements are 4-node bilinear plane strain continuum elements, CPE4RT, and 4-node linear hydrogen influenced cohesive elements, implemented along the entire crack plane length. In accordance with experimental findings, the crack path is defined 15 µm from the interface into the BM. The development of the cohesive element is described in [29], implemented in ABAQUS through the user subroutine UEL.

To ensure sufficient resolution of the local stress and strain fields, the mesh is refined at the notch tip and in the ligament until a minimum size of 7.5-15 µm. Ancillary computations have been carried out, investigating a possible influence of the mesh size by considering two crack tip element sizes: 3.75 and 7.5 µm. No influence of mesh size on the resulting CTOD level and the corresponding mechanical fields was found, deeming a minimum 7.5 µm element size sufficient.

A load (F) equal to 0.74 N/min is applied to the node corresponding to the centre of the upper pin hole, blocked from displacement in the crack growth direction, while the node corresponding to the centre of the lower pin hole is fixed, discretized as elastic material in order to avoid concentrated plastic deformation. All free surfaces of the specimen are prescribed to have a hydrogen concentration equal to C_{L0}, assumed to be constant during the entire simulation procedure. Simulations indicate that the BM is completely saturated with hydrogen upon the start of loading, consistent with preliminary computations by Fick's law.

Material properties representative of the BM and the clad are implemented into the model, summarized in Table 4. As the BM is considered the most critical material for hydrogen induced fracture under the current conditions, confirmed by the laboratory experimental testing, the values of the hydrogen related material properties are taken representative of the BM for the entire model domain, i.e. both for the BM and the clad. Material specific stress-strain curves were obtained by laboratory tensile testing of the actual materials, with the plastic part of the tensile curves given in Figure 9. The diffusion coefficient and the trap binding energy was retrieved on a X70 grade steel using the electrochemical permeation technique, previously reported by Skjellerudsveen et al. [30], while the remainder of the material parameters were taken according to literature. Unless otherwise stated, C_{L0} is assumed to be $5.13 \cdot 10^{-4}$ wppm, equal to the theoretical solubility of hy-

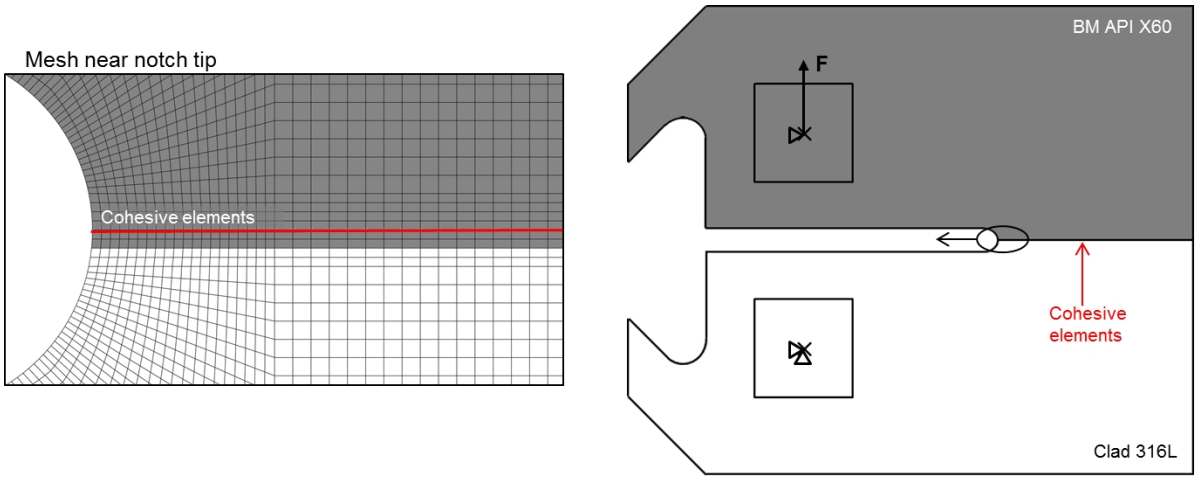

Figure 8: 2D finite element numerical model of compact tension specimen, with mechanical boundary conditions, loading and detailed mesh discretization.

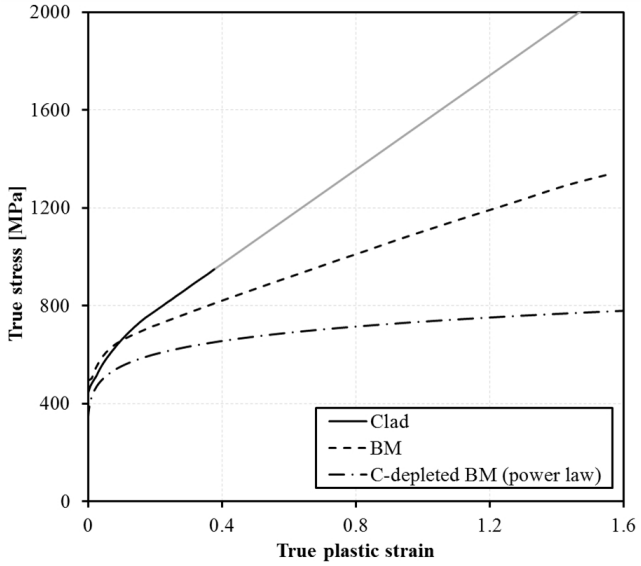

Figure 9: Plastic part of tensile curves for the clad, BM and power law BM, implemented into the FE model. Grey curves indicate a theoretical extension of the experimental curves.

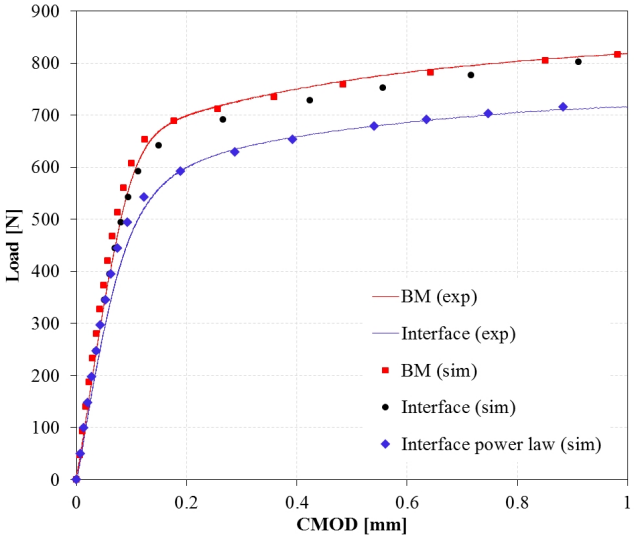

Figure 10: Load-CMOD curves for bi-material (interface) and pure BM specimens, resulting from CT fracture mechanical testing and simulations.

drogen in pure iron at 20 °C and 1 atm. pressure [31].

5.2. Verification of material model

To verify the simulations and the input material models, load-CMOD curves were calculated based on 3D elastic plastic simulations. The 3D model domain features similar characteristics as the 2D model, restricted to one half of the specimen when taking advantage of symmetry. Figure 10 presents load-CMOD curves for the bi-material (interface) and BM specimens, resulting from CT experimental fracture mechanical testing and simulations. While the model is able to reproduce the experimental curves for the pure BM samples, a lack of consistency between the experimental and simulated curves for the bi-material samples indicates limitations in the interface material model.

Carbon depletion and subsequent grain growth leads to the formation of a soft ferritic band in the BM adjacent to the clad interface, with a corresponding lowering in hard-

Table 4: Model input parameters.

Property	Unit	Symbol	Value	
			BM	Clad
Young's modulues	MPa	E	208000	167000
Poisson's ratio		ν	0.3	0.3
Diffusion coefficient	mm^2/s	D_L	$7.60 \cdot 10^{-5}$	-
Trap binding energy	kJ/mol	E_B	37	-
Molar volume of host lattice	mm^3/mol	V_M	$7.106 \cdot 10^3$	-
Partial molar volume of H	mm^3/mol	$\overline{V}_H$	$2.0 \cdot 10^3$ [32]	-
Interstitial lattice sites per host atom		β	6 [32]	-
Lattice parameter	nm	a	0.286	-
Gibbs energy	kJ/mol	ΔG_b^0	30 [10]	-

ness and tensile strength. Motarjemi et al. [4] found a decrease in the yield strength of 12% in the interface carbon depleted zone compared to the substrate BM, followed by an increase 10 mm down the BM. Pavlina and Van Tyne [33] have correlated yield strength with Vickers hardness for a range of nonaustenitic, hypoeutectoid steels, based on complied data. For non-martensitic steels, the following relationship was found:

$$\sigma_y = 2.646\text{HV} - 84.8 \quad \text{for} \quad 129 < \text{HV} < 363 \quad (15)$$

yielding a BM interface yield strength of 328 MPa for a measured hardness of 156 HV, a decrease of 33%.

In order to establish a valid material model for the bimaterial (interface) specimens, an iteration procedure has been performed, obtaining a best fit stress-strain relationship in the form of a power law. Both the material model for the clad and the elastic properties of the BM are kept unchanged. The yield strength was chosen based on Eq. (15)), i.e. 328 MPa, yielding a hardening exponent equal to 0.125. Figure 9 displays the resulting plastic part of the tensile curve, denoted C-depleted BM. The resulting simulated load-CMOD curve is included in Figure 10 as Interface power law, yielding a good fit with the experimental findings.

6. Numerical results and discussion

6.1. Identification of the cohesive parameters

The cohesive simulations are performed under the assumption that crack initiation is the critical event for total failure of the model; failure is regarded as complete separation of the first cohesive element. In the present work, damage is assumed to initiate when the maximum cohesive stress ratio reaches a value of one, a criterion represented by:

$$\max\left[\frac{\sigma(\theta_H)}{\sigma_c(\theta_H)}\right] = 1, \quad 0 \leq \theta_H \leq 1 \quad (16)$$

It is assumed that Mode I is the critical mode for failure. While interface fracture between two dissimilar materials is generally of mixed mode due to material property asymmetry, preliminary computations find the assumption of Mode I critical fracture valid for the current model.

The identification of the cohesive parameters has been conducted based on experimental CTOD fracture initiation toughness obtained in air, Table 3. Resulting values are reported in Table 5, where the initial cohesive stiffness k_n is defined by the initial slope of the polynomial TSL:

$$k_n = \frac{27}{4}\frac{\sigma_c}{\delta_c} \quad (17)$$

Table 5: Cohesive input parameters and resulting simulated fracture initiation toughness values without hydrogen.

k_n	σ_c	Γ_c	K_{Ic}	CTOD (δ_i)
[MPa/mm]	[MPa]	[N/mm]	[MPa$\sqrt{\text{m}}$]	[mm]
$4 \cdot 10^6$	1210	1.4	17.8	0.173

The value of the initial cohesive stiffness should be chosen in order to avoid artificial compliance of the model [13]; while low values of the cohesive elements initial stiffness will modify the overall compliance of the system, too high values may infer convergence problems. Following Alvaro et al. [13], an initial cohesive stiffness of $k_n = 4 \cdot 10^6$ MPa/mm was selected. Ancillary computations, investigating the influence of the initial cohesive stiffness on the resulting mechanical fields, confirmed this value suitable for the current model.

A best fit to the experimental results was achieved for a critical cohesive stress $\sigma_c = 1210$ MPa. The corresponding cohesive energy yields $\Gamma_c = 1.4$ N/mm, representing a large discrepancy with the experimental fracture initiation energy from CTOD-R testing in Table 3. Similar inconsistent findings have been reported by Moriconi et al. [14] on modelling fatigue crack propagation in high strength steels. The value is however comparable to that reported by Olden et al. [11] on cohesive modelling of fracture initiation in a rounded notch duplex stainless steel tensile specimen.

6.2. Modelling of CT testing under electrochemical hydrogen charging conditions

The finite element simulations aim to reproduce hydrogen induced crack initiation. Conforming to numerical computations without hydrogen influence, Figure 11 presents contour plots of (a) the opening stress and (b) the equivalent plastic strain, corresponding to the resulting experimental CTOD fracture initiation toughness for testing under CP (Table 3). Plots of the accompanying mechanical field profiles ahead of the notch tip are also included. While maximum opening stress is reached in the austenitic clad just adjacent to the BM, the stress gradients at the interface are generally low due to the lack of an initially sharp crack. Considering the equivalent plastic strain, the highest levels are confined to the carbon depleted BM, due to it's lower yield strength, with maximum values reached in the elements adjacent to the clad. It can be concluded that the location of maximum equivalent plastic strain corresponds well with the experimentally determined crack path, being on average 10-20 μm into the BM.

Simulation of CT fracture mechanical testing under hydrogen charging is performed as described in Section 4 and 5, with cohesive input parameters as obtained from simulations in air (Table 5). The hydrogen coverage θ_H is a function of the local hydrogen concentration in the material, which can be determined in terms of C_L, C_T or both. Various approaches are reported in literature [25, 10, 13, 14, 12].

To date, the effect of trapping on hydrogen induced fracture remains controversial and there is no consensus as to whether hydrogen in lattice or hydrogen trapped at microstructural defects is the dominant source of embrittlement. Novak et al. [25] found that high-binding energy traps ($E_B \geq 48$ kJ/mol) cannot account for the loss in strength observed on hydrogen charged steel. Similar findings have been reported by Ayas et al. [34, 35]. Rather, it is dependent on the lattice sites and low-binding energy trapping sites. While Novak et al. [25] conjectured that low-binding energy dislocations are the governing source promoting hydrogen induced fracture, Ayas et al. [34] reported the presence of lattice hydrogen to be the critical event.

In order to investigate the influence of hydrogen charging on decohesion, in the following the hydrogen coverage is determined both in terms of the lattice concentration C_L and the total concentration $C_L + C_T$, with the aim of reproducing crack initiation under CP conditions.

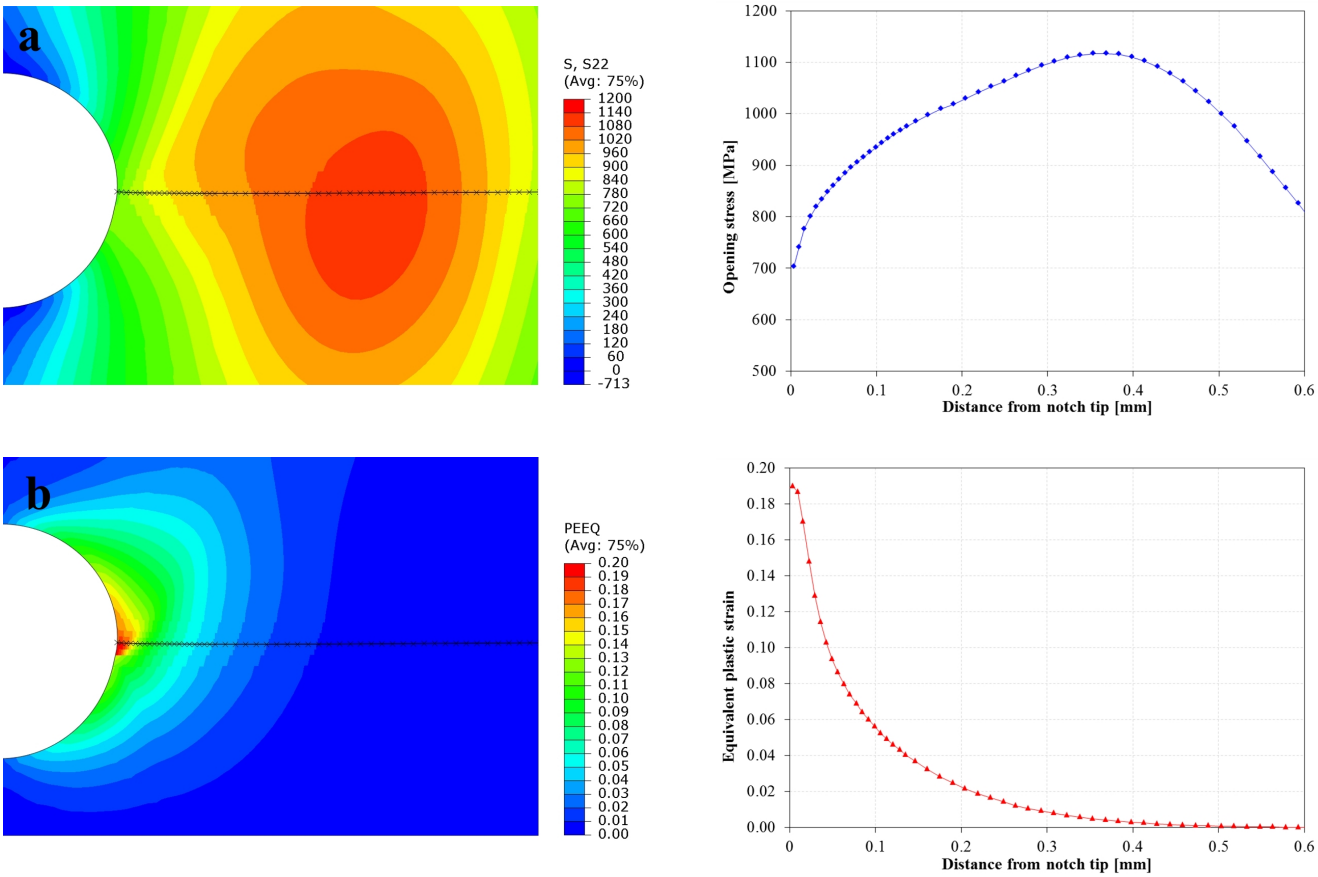

Figure 11: Contour plots and field profiles of (a) the opening stress and (b) the equivalent plastic strain, corresponding to the resulting experimental CTOD fracture initiation toughness for testing under CP. Contour Plot ligament length: 0.6 mm.

6.2.1. Influence of lattice hydrogen concentration

In the following, the hydrogen coverage θ_H is determined in terms of the lattice hydrogen concentration C_L; $C = C_L$. The results in terms of simulated CTOD fracture initiation toughness (δ_i) are reported in Table 6, for C_{L0} in the range $0.000513 - 0.5$ wppm and two trap density models.

For a constant surface hydrogen concentration equal to the theoretical solubility of hydrogen in pure iron, $C_{L0} = 5.13 \cdot 10^{-4}$ wppm, the model is not able to account for the significant reduction in fracture initiation toughness observed in the laboratory experiments, with a reduction in CTOD of only 35% compared to 85% from the fracture mechanical testing. As expected, with increasing lattice surface hydrogen concentration the CTOD level is correspondingly reduced. Assuming hydrogen in lattice to be the dominant source of embrittlement, the model predicts a lattice surface hydrogen concentration of approximately 0.005 wppm, giving a CTOD fracture initiation toughness close to the experimental findings.

Figure 12 presents the resulting hydrogen coverage profiles ahead of the crack tip for surface hydrogen concentrations of 0.00513 and 0.005 wppm, taken at the last frame before fracture initiates. The profiles are consistent with the plot in Figure 7, following the hydrostatic stress distribution in the specimen. Maximum coverage values are reached at the hydrostatic stress peaks, 1.2% and 9.6% for concentrations of 0.000513 and 0.005 wppm, respectively. For all cases considered, fracture initiated at the location of maximum opening and hydrostatic stress, a distance 0.35 mm from the notch tip when the lattice surface concentration is 0.005 wppm.

Table 6: Simulated CTOD fracture initiation toughness for $C = C_L$, with C_{L0} in the range $0.000513 - 0.5$ wppm and trap density models by Kumnick and Johnson and Sofronis et al.

C_{L0} [wppm]	CTOD (δ_i) [mm]	
	Trap model	
	Kumnick & Johnson	Sofronis et al.
0	0.173	0.173
0.000513	0.111	0.112
0.005	0.023	0.024
0.05	0.002	0.002
0.5	0.0002	0.0002

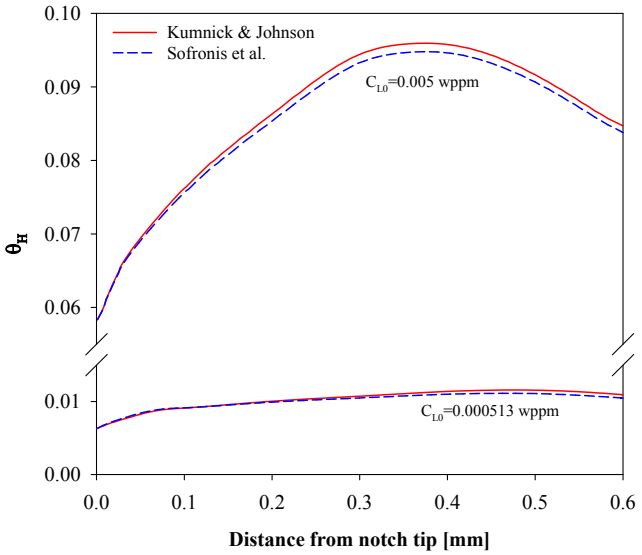

Figure 12: Hydrogen coverage profiles ahead of the crack tip for $C = C_L$, with C_{L0} of 0.000513 and 0.5 wppm and trap density models by Kumnick and Johnson and Sofronis et al. Taken at the last frame before fracture initiates.

One of the main disadvantages concerning electrochemical hydrogen charging is the lack of suitable methods for accurately estimating the hydrogen content and distribution in the material [25, 11]. Alvaro et al. [13] reported the total hydrogen concentration in a X70 grade steel to be 1.5-2.5 wppm after pre-charging in a 3% NaCl solution, measured by melt extraction. This included all the hydrogen present in the material. Retrieving the diffusion coefficient and the trap binding energy by the electrochemical permeation technique, as previously reported by Skjellerudsveen et al. [30], the estimated number of reversible traps gave $2.3 \cdot 10^{16}$ sites/mm^3 (no deformation). Assuming $C_{L0} = 0.005$ wppm, the total hydrogen concentration at the end of pre-charging can be approximated by Equation (6), giving $C_{L0} + C_{T0} = 0.76$ wppm. This amount represents the lattice and reversible trapped hydrogen content, and as such, appears reasonable when compared to the findings by Alvaro et al. [13], which also includes irreversibly trapped hydrogen.

From Table 6, it is apparent that the model predictions are not sensitive to the choice of trapping model, because there is no or negligible difference in the simulated CTOD fracture initiation toughness values. Indeed, Dadfarnia et al. [36] have reported that while a higher trap density reduces the effective diffusion coefficient of hydrogen, it has no effect on the magnitude of the steady state NILS concentration profiles. Figure 12 reveals the hydrogen coverage to be marginally lower for the Sofronis trap density model. While the maximum attained trap density equals about 600-700 times the maximum number of traps given by the Kumnick and Johnson model, the average overall lowering of the diffusivity is not sufficient to significantly reduce the hydrogen distribution prior to crack initiation. For a surface concentration of 0.005 wppm, about 95% and 96% of steady state concentration is reached at the time of fracture initiation.

6.2.2. Influence of total hydrogen concentration

In the following, the hydrogen coverage θ_H is determined in terms of the total hydrogen concentration; $C = C_L + C_T$. The results in terms of simulated CTOD fracture initiation toughness (δ_i) are reported in Table 7, for C_{L0} values of 0.000513 and 0.005 wppm and two trap density models.

Comparing the results in Table 6 and 7, it is apparent that the model predictions are not sensitive to trapped hydrogen, when determined by the Kumnick and John-

Table 7: Simulated CTOD fracture initiation toughness for $C = C_L$, with C_{L0} of 0.000513 and 0.5 wppm and trap density models by Kumnick and Johnson and Sofronis et al.

C_{L0} [wppm]	CTOD (δ_i) [mm]	
	Trap model	
	Kumnick & Johnson	Sofronis et al.
0	0.173	0.173
0.000513	0.111	0.025
0.005	0.023	0.004

son model, because there is no difference in the simulated CTOD fracture initiation toughness values. Rather, the model predicts hydrogen in lattice to be the dominant source of embrittlement, with a lattice surface hydrogen concentration of approximately 0.005 wppm giving a CTOD fracture initiation toughness close to the experimental findings.

The corresponding hydrogen coverage profiles ahead of the crack tip are presented in Figure 13a, including for comparison the results in terms of C_L, as previously reported in Figure 12. The influence of trapped hydrogen is noticed in the area immediately ahead of the notch tip, consistent with the plastic strain distribution in the sample. For $C_{L0} = 0.005$ wppm, a maximum coverage of 9.6% is reached at the hydrostatic stress peak, confirming the negligible influence of trapping on the simulated CTOD fracture initiation toughness values. With an equivalent plastic strain level less than 0.2, as according to Figure 11, the number of dislocation traps are not sufficient to significantly increase the overall hydrogen content in the specimen. A significant contribution of trapping is however noticed for $C_{L0} = 0.000531$ wppm, where a maximum coverage of 1.5% is reached just ahead of the notch tip. This is consistent with the higher reported CTOD value (Table 7), increasing the amount of plastic strain and the corresponding number of dislocation traps before fracture initiation. For both cases, fracture initiated at the location of maximum opening and hydrostatic stress, consistent with the findings in the previous section, confirming the overall negligible influence of trapped hydrogen. While trapping increased the hydrogen concentration at the notch tip beyond that found at the hydrostatic stress peak for $C_{L0} = 0.000531$ wppm, it was not sufficient to reduce the local critical cohesive stress below the opening stress.

Assuming a trap density according to the model by Sofronis et al., it is apparent from Tables 6 and 7 that trapped hydrogen impose significant influence on the model predictions, lowering the simulated CTOD fracture initiation toughness values. The model predicts hydrogen in traps to be the dominant source of embrittlement, with a lattice surface hydrogen concentration equal to the theoretical solubility of hydrogen in pure iron ($C_{L0} = 0.000531$ wppm) giving a CTOD fracture initiation toughness close to the experimental findings. The hydrogen coverage profiles in Figure 13b confirm the model predictions; trapping increases the maximum hydrogen coverage with more than 4000%. According to Oriani's theory [22], hydrogen in NILS and hydrogen in traps are always in a local equilibrium. As such, the trap site occupancy is proportional to the NILS concentration. This is actually observed in Figure 13b, where the trapped concentration for $C_{L0} = 0.005$ wppm increases beyond that for $C_{L0} = 0.000531$ wppm, despite a lower level of plastic strain.

Failure initiates once a critical combination of both opening stress and hydrogen concentration is attained. Previous authors have described the diffusion models as reflecting a competition between the plastic strain and the hydrostatic stress, determining the hydrogen distribution near a crack tip [16, 13]. In the present work, it is concluded that either lattice or trapped hydrogen plays the dominating factor, dependent on the chosen trap density model. The effect the openings stress becomes apparent when evaluating the crack initiation site. While maximum hydrogen coverage is reached at the location of maximum

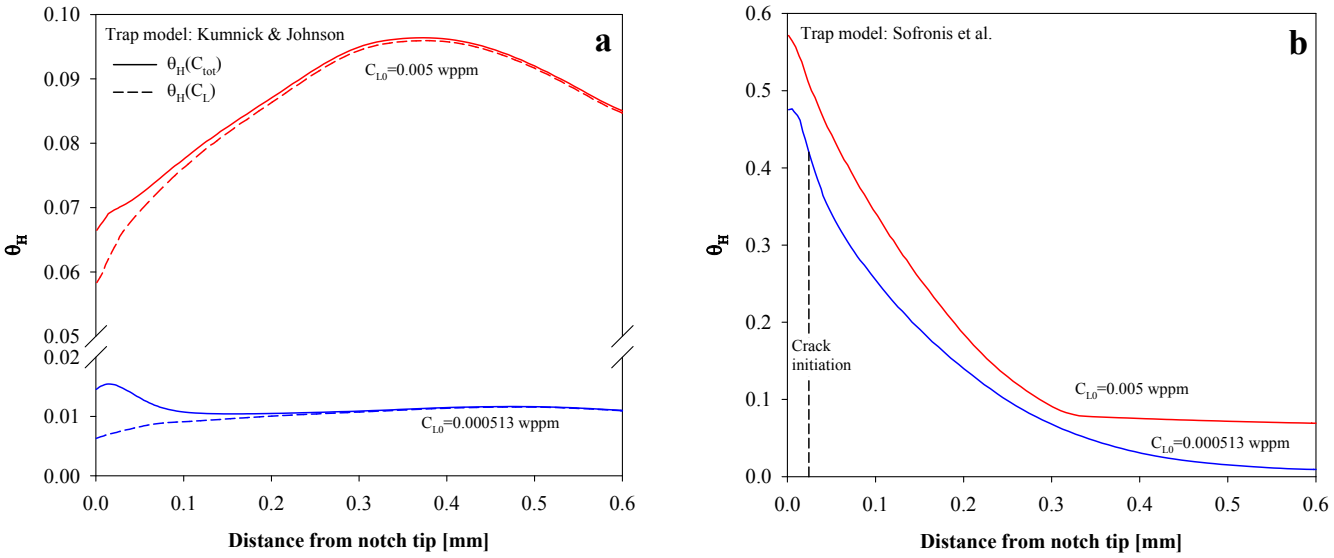

Figure 13: Hydrogen coverage profiles ahead of the crack tip for $C = C_L + C_T$, with C_{L0} of 0.000513 and 0.5 wppm and trap density models by (a) Kumnick and Johnson and (b) Sofronis et al. Taken at the last frame before fracture initiates.

plastic strain, fracture initiates a distance 24 µm into the sample where the opening stress is increased and the hydrogen concentration has sufficiently reduced the local critical cohesive stress. Crack initiation is indicated by a black dotted line in Figure 13b.

From Table 7, it can be concluded that the model predictions are particularly sensitive to the choice of trapping model, assuming both lattice and trapped hydrogen contributes to the embrittlement process, because there is significant difference in the simulated CTOD fracture initiation toughness values. This is in contradiction to the findings by Novak et al. [25], who reported no sensitivity to the trapping model in the normalized failure stress of an AISI 4340 martensitic steel, despite the trap densities being disparate. The lack of sensitivity derived from the fact that in this model, the hydrogen-induced decohesion relates to the trap occupancy, which according to the Oriani theory [22] is independent of the trap density. Previous work by the present authors [18] have shown that the choice of trapping model is only significant for dislocation trap binding energies levels above 23 kJ/mol, where trapping may yield the dominating influence on the total hydrogen concentration. For the current model, a value originally retrieved on unstrained X70 pipeline steel is applied, not representative of any specific trapping site. Dislocation trap binding energies reported in literature range from $0 - 60$ kJ/mol [18], while lower values appear more common. Recent diffusion measurements on a X65 base material suggest a trap binding energy of 15.2 kJ/mol [37], significantly lower than the current value of 37 kJ/mol. Conforming to this energy level, lattice hydrogen yield the dominating influence on the total hydrogen concentration in the specimen, independent of trap density model.

6.3. Implications of the model

The preceding results suggest that both hydrogen in lattice and hydrogen trapped at dislocations can be responsible for the observed hydrogen induced reduction in CTOD fracture initiation toughness of clad pipes. Hydrogen trapped at dislocations, as determined by the Kumnick and Johnson model, infer negligible influence on the simulated CTOD fracture initiation toughness values. It appears as one of the main challenges with the current modelling approach is the identification of valid and representative input parameters and boundary conditions for the actual system in question.

Table 8: Experimental and simulated CTOD at maximum attained load for pure BM specimens. Trap density model according to Sofronis et al.

Method	C_{L0} [wppm]	Env.	$\text{CTOD}_{\max}$ [mm]
Exp.	-	CP	0.086 ± 0.006
Sim.	0.000513	C_L	0.134
Sim.	0.000513	$C_L + C_T$	0.023
Sim.	0.005	C_L	0.015

To further investigate the models capability of predicting hydrogen induced fracture, numerical simulations of pure BM specimens were performed and compared with experimentally determined CTOD values at maximum attained load, Figure 3, as values of crack initiation are not available. The identification of the cohesive parameters was conducted as described in Section 6.1 for the bi-material samples, with an initial cohesive stiffness of $k_n = 4 \cdot 10^6$ MPa/mm. A best fit to the experimental results in air was achieved for a critical cohesive stress $\sigma_c = 1394$ MPa. Table 8 presents the results in terms of $\text{CTOD}_{\max}$ under hydrogen influence. Only the Sofronis et al. trap density model is considered. Comparing with Tables 6 and 7, it is apparent that the current modelling approach fails on transferring between different material systems, indicating limitations in the model. For the bi-material samples, the combination of residual stresses and inter metallic compounds at the interface may result in an increased initial hydrogen concentration. This is consistent with the present findings, where the model predicts a lower lattice surface hydrogen concentration for the pure BM samples. Hydrogen induced failures along dissimilar metal welds have previously been attributed to the presence of carbide precipitates at the interface, serving as traps and increasing the local hydrogen content [7, 8]. Further effort is needed to provide a reliable description of the interface hydrogen content and distribution.

Using a similar approach to model fatigue crack propagation by gaseous hydrogen in a martensitic stainless steel, Moriconi et al. [14] found that while the model was able to reasonably predict the crack growth behaviour under low hydrogen pressure, it failed to account for the enhanced crack growth observed at high pressures. Similar limitations were encountered by Alvaro et al. [13] on modelling the effect of gaseous hydrogen the fracture toughness of X70 pipeline steel. For both cases, Sievert's law was used to obtain the boundary conditions as a function of the external hydrogen pressure. Limitations in the model, particular in the case of lattice diffusion, were pointed out as possible explanations, while no conclusions were drawn. By also including the effect of hydrogen on the local yield strength, Brocks et al. [12] have simulated CTOD-R curves for various deformations rates on a high strength low alloy steel. The results indicate that only a combined mechanism of hydrogen reduced cohesive strength and hydrogen reduced yield strength can give reasonable predictions according to experimental findings.

Finally, it should be noticed that when trapped hydrogen is not taken into account, fracture initiates at the opening stress peak, about 0.35 mm from the notch. These findings are inconsistent with the results from the experimental fracture mechanical testing [9], where failure initiates closer to the notch tip both in air and with hydrogen influence. This could indicate limitations in cohesive model's capability of predicting crack initiation in front of a rounded notch, and is a topic for further investigation.

7. Conclusion

A combined experimental and finite element cohesive zone modelling approach for prediction of hydrogen induced fracture initiation in a hot roll bonded clad steel pipe is proposed. The developed model is based on coupled effects between mechanical loading and hydrogen mass diffusion. The main results are summarised as follows:

- A best fit to the experimental results in air was achieved

for an initial cohesive stiffness $k_n = 4{\cdot}10^6$ MPa/mm and a critical cohesive stress $\sigma_c = 1210$ MPa.

- The simulated results reveals that both hydrogen in lattice and hydrogen trapped at dislocations can be responsible for the observed hydrogen induced reduction in CTOD fracture initation toughness of clad pipes.
- Assuming hydrogen in lattice to be the dominant source of embrittlement, the model predictions are insensitive to the choice of trap density formulation. A best fit to the experimental CTOD fracture initiation toughness was achieved for a lattice surface hydrogen concentration of 0.005 wppm.
- Assuming both lattice and trapped hydrogen to infer an influence on the hydrogen reduced cohesive strength, the model predictions are particularity sensitive to the choice of trap density formulation:
  - The Kumnick and Johnson model: Hydrogen trapped at dislocations infer negligible influence on the simulated CTOD fracture initiation toughness. The model predicts hydrogen in lattice to be the dominant source of embrittlement, with a best fit to the experimental results achieved for a lattice surface hydrogen concentration of 0.005 wppm.
  - The Sofronis et al. model: Hydrogen trapped at dislocations infer significant influence on the simulated CTOD fracture initiation toughness, increasing the hydrogen coverage with more than 4000%. The model predicts hydrogen in traps to be the dominant source of embrittlement, with a best fit to the experimental results achieved for a lattice surface hydrogen concentration of 0.000531 wppm.
- The present modelling approach fails on transferring between different material systems. Further effort is needed to provide a reliable description of the interface hydrogen content and distribution.

Acknowledgements

The present work was financed by the Research Council of Norway (Petromaks 2 programme, Contract No. 234110 /E30), Statoil, Gassco, Technip, POSCO and EDF Induction and performed within the frames of the ROP project (www.sintef.no/rop). The authors gratefully acknowledge the valuable input from Antonio Alvaro and Vidar Osen.

References

[1] L. Smith, M. Celant, CASTI handbook of cladding technology, 2nd Edition, CASTI Publishing Inc., 2000.

[2] T. Reichel, J. Beissel, V. Pavlyk, G. Heigl, Production of metallurgically cladded pipes for high end applications in the oil & gas industry, in: Proc. ASME 27th Int. Conf. Offshore Mech. Arct. Eng., 2008, pp. 179–186. doi:10.1115/OMAE2008-57311.

[3] S. Missori, F. Murdolo, A. Sili, Microstructural characterization of a stainless-cladded carbon steel, Metall. Sci. Technol. 19 (2) (2001) 21–24.

[4] A. Khodadad Motarjemi, M. Koçak, V. Ventzke, Mechanical and fracture characterization of a bi-material steel plate, Int. J. Press. Vessel. Pip. 79 (3) (2002) 181–191. doi:10.1016/S0308-0161(02)00012-1.

[5] H. Bjaaland, O. M. Akselsen, V. Olden, B. Nyhus, M. Karlsen, J. Hjelen, Metallurgical reactions in welding of clad X60 / X65 pipelines, Proc. Twenty-fifth Int. Ocean Polar Eng. Conf. (2015) 61–66.

[6] Z. Dhib, N. Guermazi, M. Gaspérini, N. Haddar, Cladding of low-carbon steel to austenitic stainless steel by hot-roll bonding: Microstructure and mechanical properties before and after welding, Mater. Sci. Eng. A 656 (2016) 130–141. doi:10.1016/j.msea.2015.12.088.

[7] J. A. Fenske, I. M. Robertson, R. Ayer, M. Hukle, D. Lillig, B. Newbury, Microstructure and hydrogen-induced failure mechanisms in Fe and Ni alloy weldments, Metall. Mater. Trans. A 43 (9) (2012) 3011–3022. doi:10.1007/s11661-012-1129-1.

[8] M. F. Dodge, H. B. Dong, M. F. Gittos, T. Mobberley, Fusion zone microstructure associated with embrittlement of subsea dissimilar joints, Proc. ASME 33rd Int. Conf. Ocean. Offshore Arct. Eng. 5. doi:10.1115/OMAE2014-23643.

[9] L. Jemblie, H. Bjaaland, B. Nyhus, V. Olden, O. M. Akselsen, Fracture toughness and hydrogen embrittlement susceptibility on the interface of clad steel pipes with and without a Ni-interlayer, Mater. Sci. Eng. A 685 (2017) 87–94. doi:10.1016/j.msea.2016.12.116.

[10] A. Serebrinsky, E. A. Carter, M. Ortiz, A quantum-mechanically informed continuum model of hydrogen embrittlement, J. Mech. Phys. Solids 52 (2004) 2403–2430. doi:10.1016/j.jmps.2004.02.010.

[11] V. Olden, C. Thaulow, R. Johnsen, E. Østby, T. Berstad, Application of hydrogen influenced cohesive laws in the prediction of hydrogen induced stress cracking in 25%Cr duplex stainless steel, Eng. Fract. Mech. 75 (8) (2008) 2333–2351. doi:10.1016/j.engfracmech.2007.09.003.

[12] W. Brocks, R. Falkenberg, I. Scheider, Coupling aspects in the simulation of hydrogen-induced stress-corrosion cracking, Procedia IUTAM 3 (2012) 11–24. doi:10.1016/j.piutam.2012.03.002.

[13] A. Alvaro, V. Olden, O. M. Akselsen, 3D cohesive modelling of hydrogen embrittlement in the heat affected zone of an X70 pipeline steel - Part II, Int. J. Hydrogen Energy 39 (2014) 3528–3541. doi:10.1016/j.ijhydene.2013.12.097.

[14] C. Moriconi, G. Hénaff, D. Halm, Cohesive zone modeling of fatigue crack propagation assisted by gaseous hydrogen in metals, Int. J. Fatigue 68 (2014) 56–66. doi:10.1016/j.ijfatigue.2014.06.007.

[15] A. Needleman, A continuum model for void nucleation by inclusion debonding, J. Appl. Mech. 54 (3) (1987) 525–531. doi:10.1115/1.3173064.

[16] P. Sofronis, R. McMeeking, Numerical analysis of hydrogen transport near a blunting crack tip, J. Mech. Phys. Solids 37 (3) (1989) 317–350. doi:10.1016/0022-5096(89)90002-1.

[17] A. Krom, R. Koers, A. Bakker, Hydrogen transport near a blunting crack tip, J. Mech. Phys. Solids 47 (4) (1999) 971–992. doi:10.1016/S0022-5096(98)00064-7.

[18] L. Jemblie, V. Olden, O. Akselsen, A coupled diffusion and cohesive zone modelling approach for numerically assessing hydrogen embrittlement of steel structures, Int. J. Hydrogen Energydoi:10.1016/j.ijhydene.2017.02.211.

[19] A. S. Azar, Characterization of Oil & Gas Clad Pipelines, Tech. Rep. SINTEF A26507, SINTEF Materials and Chemistry (2014).

[20] Y. Lee, R. P. Gangloff, Measurement and modeling of hydrogen environment–assisted cracking of ultra-high-strength steel, Metall. Mater. Trans. A 38 (13) (2007) 2174–2190. doi:10.1007/s11661-006-9051-z.

[21] British Standard BS 7448-4, Fracture mechanics toughness tests - Part 4: Method for determination of fracture resistance curves and initiation values for stable crack extension in metallic materials (1997).

[22] R. A. Oriani, The diffusion and trapping of hydrogen in steel, Acta Metall. 18 (1) (1970) 147–157. doi:10.1016/0001-6160(70)90078-7.

[23] A. Kumnick, H. Johnson, Deep trapping states for hydrogen in deformed iron, Acta Metall. 28 (1) (1980) 33–39. doi:10.1016/0001-6160(80)90038-3.

[24] P. Sofronis, Y. Liang, N. Aravas, Hydrogen induced shear localization of the plastic flow in metals and alloys, Eur. J. Mech. A - Solids 20 (2001) 857–872. doi:10.1016/S0997-7538(01)01179-2.

[25] P. Novak, R. Yuan, B. P. Somerday, P. Sofronis, R. O. Ritchie, A statistical, physical-based, micro-mechanical model of hydrogen-induced intergranular fracture in steel, J. Mech. Phys. Solids 58 (2) (2010) 206–226. doi:10.1016/j.jmps.2009.10.005.

[26] A. Alvaro, P. Mainçon, V. Osen, FEM formulation for mass diffusion through UMATHT subroutine, Tech. Rep. SINTEF A26585, SINTEF (2015).

[27] D. E. Jiang, E. A. Carter, First principles assessment of ideal fracture energies of materials with mobile impurities: implications for hydrogen embrittlement of metals, Acta Mater. 52 (2004) 4801–4807. doi:10.1016/j.actamat.2004.06.037.

[28] E. D. Hondros, M. P. Seah, The theory of grain boundary segregation in terms of surface adsorption analogues, Metall. Trans. A 8 (9) (1977) 1363–1371. doi:10.1007/BF02642850.

[29] P. Mainçon, Cohesive zone element, Tech. Rep. SINTEF F28059, SINTEF (2017).

[30] M. Skjellerudsveen, O. M. Akselsen, V. Olden, R. Johnsen, A. Smirnova, The effect of microstructure and temperature on hydrogen diffusion in X70 grade pipeline steel and its weldments, in: EUROCORR, 2010.

[31] A. Turnbull, Hydrogen diffusion and trapping in metals, in: Gaseous Hydrog. Embrittlement Mater. Energy Technol., Elsevier, 2012, pp. 89–128. doi:10.1533/9780857095374.1.89.

[32] J. P. Hirth, Effects of hydrogen on the properties of iron and steel, Metall. Trans. A 11 (6) (1980) 861–890. doi:10.1007/BF02654700.

[33] E. J. Pavlina, C. J. Van Tyne, Correlation of Yield Strength and Tensile Strength with Hardness for Steels, J. Mater. Eng. Perform. 17 (6) (2008) 888–893. doi:10.1007/s11665-008-9225-5.

[34] C. Ayas, V. S. Deshpande, N. A. Fleck, A fracture criterion for the notch strength of high strength steels in the presence of hydrogen, J. Mech. Phys. Solids 63 (2014) 80–93. doi:10.1016/j.jmps.2013.10.002.

[35] C. Ayas, N. A. Fleck, V. S. Deshpande, Mechanics of Materials Hydrogen embrittlement of a bimaterial, Mech. Mater. 80 (2015) 193–202. doi:10.1016/j.mechmat.2014.06.002.

[36] M. Dadfarnia, P. Sofronis, T. Neeraj, Hydrogen interaction with multiple traps: Can it be used to mitigate embrittlement?, Int. J. Hydrogen Energy 36 (16) (2011) 10141–10148. doi:10.1016/j.ijhydene.2011.05.027.

[37] J. Yamabe, Unpublished work Kyushu University/I2CNER (2016).